Evolution of structure and anisotropic shear stiffness of compacted loess during compression

Authors: Bao-Lin Dai, Chao Zhou*, Qing-Yi Mu and Jian-Bing Peng

*Corresponding author

Information of the authors:

First author: Mr. Bao-Lin Dai

PhD student, Department of Civil and Environmental Engineering, The Hong Kong Polytechnic University, Hung Hom, Hong Kong. E-mail: baolin.dai@connect.polyu.hk

Corresponding author: Dr Chao Zhou

Tsui Tack Kong Young Scholar in Civil Engineering, Associate Professor, Department of Civil and Environmental Engineering, The Hong Kong Polytechnic University, Hung Hom, Hong Kong. E-mail: c.zhou@polyu.edu.hk

Co-author: Dr Qing-Yi Mu

Professor, School of Geological Engineering and Geomatics, Chang'an University, Xi'an, 710053, China. E-mail: qingyimu@chd.edu.cn

Co-author: Dr Jianbing Peng

Professor, School of Geological Engineering and Geomatics, Chang'an University, Xi'an, 710049, China. E-mail: dicexy_1@126.com

Abstract

Different compaction conditions (water content and density) may induce various soil structures. The influence of these structures on small strain shear stiffness G seems contradictory and is not understood (e.g., denser specimens may have larger or smaller G than looser specimens after compression). Furthermore, the influence of compaction condition on stiffness anisotropy remains unclear. This study investigated the evolution of structure and anisotropic stiffness of saturated and compacted loess during isotropic compression. Specimens compacted at different water contents and densities were explored. The measured G was normalised by a void ratio function ($f(e)$) to eliminate density effects. Before yielding, $G/f(e)$ increases with decreasing compaction water content and increasing density. These two trends are reversed at large stresses (2 to 3 times yield stress), implying that an initially softer structure becomes stiffer. Based on MIP, SM and SEM results, the trend reversal is likely because interparticle contacts are more strengthened and pores are more compressed in the initially softer specimens. Furthermore, the stiffness anisotropy becomes more significant with decreasing compaction water content and increasing density because of more orientated fabrics, as evidenced by the particle/aggregate directional distribution results.

Keywords: small strain shear stiffness; structure; anisotropy; loess

Introduction

It has been recognised that different compaction conditions (compaction water content and dry density) can induce various soil structures, which significantly affects the engineering properties of soils (Delage et al., 1996; Mitchell and Soga, 2005; Alonso et al., 2013). So far, some researchers have studied the influence of compaction condition on the shear stiffness G at very small strains (0.001% or less), which is a crucial parameter for calculating ground movement and analysing geo-structure performance under working conditions (Atkinson, 2000; Gasparre et al., 2007; Ng and Menzies, 2007; Clayton, 2011; Bentil and Zhou, 2024; Zuo et al., 2024; Dai and Zhou, 2025). Mancuso et al. (2002) investigated the evolution of G for optimum and wet of optimum compacted specimens during isotropic compression. It was found that soil fabric became softer with increasing compaction water content. Under the saturated condition, the wet of optimum compacted specimen had about 50% and 20% smaller G than the optimum compacted specimen at mean effective stress (p') of 1 and 400 kPa, respectively. Wang et al. (2022) explored the stiffness G of compacted granite prepared at different dry densities. The results showed that G increased by about 20% when the compaction dry density increased from 1.60 to 1.92 g/cm^3. In contrast, Todisco et al. (2018) found that the denser and looser Leighton Buzzard sand had identical G although their void ratios were different (Δe = 0.10). Wang et al. (2021) investigated the G of saturated and compacted loess with p' increasing from 40 kPa to 1200 kPa. The denser specimen had about 20% larger G than the looser specimen at p' of 40 kPa. However, the trend was reversed when p' exceeded 800 kPa, with a smaller G in the denser specimen than the looser one.

The above results suggest that the stiffness G is affected by compaction condition, but inconsistent results are identified. For example, the denser specimens could have larger, similar or smaller G than the looser specimens although the void ratio is smaller in the former. This conclusion remains valid when comparing the stiffness normalised by a void ratio function (i.e., $G/f(e)$). So far, possible explanations for the inconsistent effects of compaction condition on stiffness are still absent. In addition to G, it has been acknowledged that the stiffness anisotropy is dependent on the compaction condition. For example, Hasan and Wheeler (2014) revealed that stiffness anisotropy increased with increasing compaction dry density. However, Hasan and Wheeler (2014) only reported the results at the as-compacted state and the suction effects cannot be eliminated during result interpretations. The influence of compaction condition on stiffness anisotropy remains unclear.

Loess is widely distributed in Asia, Europe, North America and Africa, covering approximately 10% of the Earth's surface (Muñoz-Castelblanco et al., 2012; Sadeghi, 2016; Mu et al., 2022). Since loess is usually characterised by an orientated soil fabric and a metastable and highly porous structure (Liu et al., 2016; Lu et al., 2019; Mu et al., 2023), studies on its small strain stiffness evolution are expected to guide the serviceability design of earthen structures in the loess area.

This study investigated the evolution of structure and anisotropic stiffness of saturated and compacted loess during isotropic compression. Specimens compacted at different water contents and dry densities were explored. The stiffness in the horizontal and vertical planes (i.e., G_{hh} and G_{hv}) were measured. To investigate the structure evolutions, stereomicroscope

(SM, an optical microscope), scanning electron microscope (SEM) and mercury intrusion porosimetry (MIP) tests were carried out on specimens before and after compression.

Tested soil and specimen preparation

Properties of the tested soil

The tested loess was sampled from Xi'an, Shaanxi province of China. Soil samples were retrieved at a depth of 1.5 m from an excavated pit. Based on laboratory tests (ASTM, 2017b, 2023), the specific gravity, liquid limit and plastic limit are 2.67, 31% and 18%, respectively. Fig. 1(a) shows the particle size distribution measured by wet sieving and hydrometer (ASTM, 1998). The clay, silt and sand contents are 25.1%, 73.7% and 1.2%, respectively. More physical properties are summarised in Table 1. According to the Unified Soil Classification System (ASTM, 2017a), this soil is classified as clay of low plasticity (CL).

Specimen preparation

Compacted specimens with 76 mm in diameter and height were prepared. To prepare compacted specimens, the oven-dried soil was broken up with a rubber hammer and de-aired water was sprayed over the soil powder step by step. Between each step, the soil was mixed thoroughly with water and any clod was broken up to achieve a uniform water distribution. As the predefined water content was achieved, the soil was sieved through a 2 mm aperture sieve to reduce the clod size. The soil was then sealed inside a plastic bag for 24 hours for moisture equalisation before static compaction in a split mould.

The static compaction method was used to compact the soil inside a ring with a loading

rate of 1 mm/min. Compaction was conducted in three layers, with scarification between layers to ensure specimen homogeneity. For each layer, the compaction was stopped when the target dry density was achieved. The maximum vertical stress for compacting each specimen was summarised in Table 2. As expected, the required vertical stress increased with increasing compaction dry density and decreasing compaction water content.

To prepare specimens for microstructural analysis, the freeze-drying method was adopted for dehydration. Small cubes with an approximate volume of 10^{-6} m^3 were retrieved from the specimens before and after compression. The cubes were first dipped into liquid nitrogen to preserve their structures and placed into a freeze dryer to remove frozen water through a sublimation mechanism. The drying process lasted for 24 hours, after which the cubes were used for structure analysis.

Test program, apparatus and procedures

Test program

Isotropic compression tests were carried out in this study, as summarised in Table 2. Specimens compacted at different water contents and dry densities were tested. The initial states of compacted specimens are shown in Fig. 1(b). Three water contents (i.e., 13.0%, 15.2% and 18.9%) and two dry densities (i.e., 1.21 and 1.52 g/cm^3) were considered. The water contents correspond to the dry of optimum, optimum and wet of optimum (denoted as 'D, O and W' in Table 2), respectively. The looser and denser states ('L and D' in Table 2) correspond to 70% and 85% degrees of compaction, respectively.

As shown in Table 3, SM, SEM and MIP tests were carried out to investigate the influence of structure on stiffness evolutions. The CWD and CDD were compared to reveal the influence of compaction water content, while the CWD and CWL were used to investigate the influence of compaction dry density. The SM and SEM were employed to observe particle arrangements at relatively small (i.e., 24×) and large (i.e., 2000×) magnifications, respectively. The microstructure of each specimen was investigated before and after compression.

Test apparatus

This study utilised a modified triaxial system (Ng and Yung, 2008; Ng et al., 2009) to conduct isotropic compression tests. The volumetric change and axial strain were continuously recorded by Global Digital System (GDS) volume controllers and linear variable differential transformers (LVDT), respectively. Two pairs of bender elements equipped with the shear wave generating and measuring systems were employed to measure the shear wave velocity and determine the small strain shear stiffness. Bender elements were installed at the mid-height of each specimen with silicon grommets.

The apparatus used for the SM, SEM and MIP tests were the Nikon SMZ1270, VEGA3 TESCAN and PoreMaster 33, respectively. The magnifications of SM and SEM equipment range from 6× to 48× and 30× to 50000×, respectively. The maximum intrusion pressure of MIP equipment is about 230 MPa.

Test procedures

After specimens were set up in the triaxial cell, they were saturated with a back pressure of 150 kPa. The B values of all specimens were above 0.95. After saturation, each specimen

144 was isotropically compressed at the drained condition with the following stages: 8, 16, 30, 50,
145 100, 200, 300 and 400 kPa. As equilibrium was reached at each stage, the axial and volumetric
146 strains were recorded and the shear wave travel times in the horizontal and vertical planes (i.e.,
147 t_{hh} and t_{hv}) were determined using the peak-to-peak method (Lee and Santamarina, 2005).
148 The travel times t_{hh} and t_{hv} were measured with a pair of horizontally embedded bender
149 elements. In the case of t_{hh}, the shear wave propagates and vibrates horizontally, while the
150 shear wave propagates horizontally but vibrates vertically for t_{hv}. The stiffness is calculated
151 using

152
$$\begin{cases} G_{hh} = \rho \left(\frac{L}{t_{hh}}\right)^2 \\ G_{hv} = \rho \left(\frac{L}{t_{hv}}\right)^2 \end{cases} \quad (1)$$

153 where ρ is the bulk density; L is the distance between the tips of two bender elements.
154 Following the test program in Table 3, the compressed specimens were unloaded and
155 dismantled from the triaxial cell and cut into small cubes for SM, SEM and MIP tests. Note
156 that the volumetric strain was relatively small during unloading (about 3%), suggesting that the
157 disturbance on the specimen was minimized and the structure features were representative of
158 the loaded state.
159
160 **Interpretations of isotropic compression behaviour**
161 Fig. 2 shows the influence of compaction water content and dry density on the isotropic
162 compression behaviour. The yield stress increases with decreasing compaction water content.
163 The specimen compacted at a lower water content can sustain a larger void ratio at a given

stress after yielding, which was attributed to different structures at different compaction water contents, as explained later. As expected, Fig. 2 shows that denser specimens have larger yield stress than looser specimens at a given compaction water content. The compression curves at looser and denser states become almost parallel when the applied stress exceeds the yield stress. In the considered stress range, the tested loess shows a transitional mode behaviour, for which the normal compression lines of specimens with different initial densities do not converge towards the same volume (Δe is about 0.15 in this study) (Martins et al., 2001). The transitional mode for saturated loess has been reported in previous studies such as Lee (2004) (Δe = 0.05) and Xu and Coop (2017) (Δe = 0.1). One postulation for the transitional mode is that strong fabrics at the microscale are difficult to break down (Todisco et al., 2018).

Interpretations of anisotropic stiffness characteristics

Under isotropic stress states, the relationship between stiffness, mean effective stress p' and void ratio e is often described using the following equation (e.g., Viggiani and Atkinson, 1995; Mitchell and Soga, 2005; Zuo et al., 2024):

$$\begin{cases} \frac{G_{hh}}{p_r} = A_{hh} f(e) \left(\frac{p'}{p_r}\right)^{n_h} \\ \frac{G_{hv}}{p_r} = A_{hv} f(e) \left(\frac{p'}{p_r}\right)^{(n_h+n_v)/2} \end{cases} \quad (2)$$

where A_{hh}, A_{hv}, n_h and n_v are model parameters; p_r is the reference pressure (taken as 1 kPa in this study); $f(e)$ is a void ratio function, which could take the simple form of $e^{-1.3}$ for fine-grained soils (e.g., Jamiolkowski et al., 1995; Zuo et al., 2024). The following discussion analyses the stiffness with and without normalised by the void ratio function (i.e., G_{hv} and

184 $G_{hv}/f(e)$). Note that the analyses and conclusions are still valid when alternative void ratio
185 functions, such as $\frac{(2.17-e)^2}{1+e}$ (Iwasaki and Tatsuoka, 1977; Liu et al., 2019) and $(1+e)^{-3}$
186 (Oztoprak and Bolton, 2013; Zhou et al., 2015), are employed.

187 *Influence of compaction dry density on the stiffness evolution*

188 Fig. 3 shows the influence of compaction dry density on the anisotropic stiffness. Before
189 compression, the G_{hv} of denser specimens is about 140%, 100% and 60% larger than that of
190 looser specimens compacted at the dry of optimum, optimum and wet of optimum, respectively.
191 As stress increases, the G_{hv} values of looser and denser specimens progressively become
192 almost identical, although different void ratios are still observed (see Fig. 2). The results that
193 looser and denser specimens have nearly identical stiffness were also reported by Todisco et
194 al. (2018) for Leighton Buzzard quartz sand (Δe = 0.1). The possible reason for the identical
195 stiffness under different void ratios is given based on the SEM and MIP analysis.

196 Fig. 4 shows the SEM results of wet of optimum specimens compacted at looser and denser
197 states (i.e., CWL and CWD). For each sample, three SEM images taken from random locations
198 are exhibited. Before compression, Fig. 4(a) and (b) show that the silt particles are coated by
199 clay particles, and abundant interparticle pores are observed. These interparticle pores are
200 compressed and interparticle contacts are enhanced after compression, as shown in Fig. 4(c)
201 and (d). Comparing the SEM results between looser and denser specimens after compression
202 (Fig. 4(c) and (d)), qualitatively comparable particle contacts are observed.

203 Fig. 5 shows the pore size distributions (PSDs) of looser and denser specimens before and
204 after compression. Fig. 5(a) reveals that both looser and denser specimens show multi-modal

PSDs before compression. The pores with dominate diameters of about 100 μm correspond to the inter-clod pores, which is induced by the relatively larger compaction water content and is also observed in compacted loess by Zhan et al. (2014). The dominant inter-clod pore diameter decreases from 110 μm to 70 μm with increasing density, leading to a larger stiffness in the denser specimen before compression. Moreover, increasing density has limited impacts on the pores with diameter less than 10 μm, which is consistent with the observation in SEM results (Fig. 4). With increasing stress from 1 to 400 kPa, the multi-modal PSDs are compressed to bi-modal PSDs for both looser and denser specimens, as shown in Fig. 5(b). Compared to the denser specimen, more pores with a dominant diameter of 0.3 μm exist for the looser specimen.

Based on the SEM results shown in Fig. 4, the different PSDs between looser and denser specimens after compression have limited effects on the interparticle contacts. Previous studies have illustrated that interparticle contact is the governing factor for stiffness G (Cascante and Santamarina, 1996; Tang et al., 2011; Asadi et al., 2020; Khosravi et al., 2020; Vahedifard et al., 2020; Akin et al., 2021; Ying et al., 2021). Therefore, the comparable interparticle contacts lead to a similar G_{hv} in looser and denser specimens after compression. Comparing Fig. 5(a) and (b), it can be concluded that more pores are compressed in the looser specimen than the denser specimen. The more compressed pores in the looser specimen are corresponding to its larger volumetric strains (Fig. 2) and more significant increases in $G_{hv}/f(e)$ (Fig. 3) than the denser specimen.

Influence of compaction dry density on the stiffness anisotropy

Fig. 6 shows the variation of stiffness anisotropy G_{hh}/G_{hv} with stress for all compacted

specimens. At the same compaction water content, stiffness anisotropy is more predominant in the denser specimens than the looser specimens, which is because soil particles/aggregates become more horizontally orientated with increasing compaction effort. As isotropic stress increases, the ratio G_{hh}/G_{hv} changes towards unit for all specimens, indicating that the soil fabric becomes isotropically distributed. The stress corresponding to a unit value of G_{hh}/G_{hv} for denser specimens is about 100 to 200 kPa, which is approximately five times larger than the yield stress. The above observations indicate that particle orientation can be completely changed as stress is larger than five times the yield stress. This stress range is similar to the results of Mitaritonna et al. (2014), who observed that a complete modification of stiffness anisotropy in the reconstituted Lucera clay can be achieved when the applied stress was four times larger than its yield stress.

Influence of compaction water content on the stiffness evolution

Fig. 7(a) and (b) show the influence of compaction water content on the stiffness (G_{hv} and $G_{hv}/f(e)$) at looser and denser states, respectively. It can be observed that the influence of compaction water content on G_{hv} and $G_{hv}/f(e)$ follows the same trend, thus the following analysis mainly focuses on the normalised stiffness. Before compression, the $G_{hv}/f(e)$ decreases with increasing compaction water content. The wet of optimum specimens have about 5% and 25% smaller $G_{hv}/f(e)$ than the dry of optimum specimens at looser and denser states, respectively. The trend is reversed when stress increases to 400 kPa, where $G_{hv}/f(e)$ increases with increasing compaction water content. At the post-compression state, the wet of optimum specimens have about 25% and 30% larger $G_{hv}/f(e)$ than the dry of optimum

247 specimens at looser and denser states, respectively. The $G_{hv}/f(e)$ decreases with increasing
248 compaction water content has been observed in previous studies such as Mancuso et al. (2002).
249 However, the wet of optimum specimen with a larger $G_{hv}/f(e)$ than the dry of optimum
250 specimen has not been reported. Fig. 8 shows the variations of parameters A_{hv} and $\frac{n_h+n_v}{2}$ with
251 compaction water content. The values of these two parameters are obtained from the results in
252 Fig. 7. The parameter A_{hv} decreases and $\frac{n_h+n_v}{2}$ increases with increasing compaction water
253 content for both looser and denser specimens. The variation of A_{hv} suggests that the stiffness
254 before compression decreases with increasing compaction water content. The variation of
255 $\frac{n_h+n_v}{2}$ indicates that the stiffness increases more significantly with stress for the specimen with
256 a larger compaction water content, which is consistent with the observation in Fig. 7. To reveal
257 the underlying mechanism for the above observations (i.e., the initial stiffness and stiffness
258 evolution), the influence of compaction water content on the soil structure is investigated, as
259 shown in Figs. 9 and 10.

260 Fig. 9 shows the SM (i.e., ×24) and SEM (i.e., ×2000) results of denser specimens
261 compacted at different water contents. Similar to Fig. 4, three images at different random
262 positions are given for each sample. As shown in the SM results given in Fig. 9(a) and (b), the
263 soil clod size increases with increasing compaction water content. For the wet of optimum
264 specimen, soil clods larger than 1000 μm and inter-clod pores of about several hundred
265 micrometers are observed. As shown in the SEM results (Fig. 9(c) and (d)), the dry of optimum
266 specimen shows an aggregated structure and abundant interaggregate pores of about 10 μm are
267 observed. In contrast, the silt particles are coated by clay particles for the wet of optimum

specimen. Similar SEM results are also reported in Delage et al. (1996), who observed aggregated structure for the dry of optimum specimen, and silt particles enveloped by clay for the wet of optimum specimen. The SM and SEM results imply that increasing compaction water content converts the "aggregated structure" to the "structure featured by clods".

Fig. 10(a) shows the PSDs of specimens with different compaction water contents before compression. The dry of optimum specimen has a dominant pore diameter of 12 μm, which corresponds to the interaggregate pores observed in SEM results (Fig. 9(b)). While the wet of optimum specimen has a peak at a diameter of 70 μm, which corresponds to the inter-clod pores observed in SM results (Fig. 9(a)). Fig. 10(b) compares the PSDs of dry and wet of optimum specimens at the post-compression state. The relatively large pores (i.e., the pores at 12 μm and 70 μm) are compressed after compression. More importantly, the PSD of the wet of optimum specimen is more significantly altered than the dry of optimum specimen with increasing stress, demonstrated by its larger inter-clod pores before compression but fewer pores between 1 to 10 μm after compression. Similarly, Oualmakran et al. (2016) observed that the dry of optimum specimen had larger pores than the wet of optimum specimen after isotropic compression with a mean effective stress of 1600 kPa.

Based on the SM, SEM and MIP results, the influence of compaction water content on the initial stiffness and its evolution can be explained. The 1-D compaction for the wet of optimum specimens induces a structure featured by clods (Fig. 9). The inter-clod pores are much larger (see Fig. 10) and more easily compressed (see Fig. 2) than the interaggregate pores in the dry of optimum specimens. Therefore, the wet of optimum specimens before compression are

289 softer than the dry of optimum specimens, resulting in a smaller $G_{hv}/f(e)$ in the former, as
290 shown in Fig. 3. With increasing stress, the more compressed pores and thus more strengthened
291 interparticle contacts for the wet of optimum specimens induces more sensitive $G_{hv}/f(e)$ to
292 stress (i.e., larger $\frac{n_h+n_v}{2}$ value in Fig. 8) and larger $G_{hv}/f(e)$ after compression (Fig. 3) than
293 the dry of optimum specimens.

294 *Influence of compaction water content on the stiffness anisotropy*

295 The variation of stiffness anisotropy G_{hh}/G_{hv} with compaction water content can be
296 identified from Fig. 6. Before compression, the stiffness anisotropy is more significant with
297 decreasing compaction water content. At the denser state, the G_{hh}/G_{hv} is 0.70, 0.89 and 0.91
298 for specimens compacted at dry of optimum , optimum and wet of the optimum, respectively.
299 With increasing stress, the G_{hh}/G_{hv} changes towards unit for all specimens, but a larger stress
300 is required for the dry of optimum specimens. The required larger stress is mainly attributed to
301 its more predominantly initial anisotropy. The results suggest that variation in the compaction
302 water content not only has an impact on the stiffness but also the stiffness anisotropy.

303 To reveal the mechanism for the influence of compaction water content on the stiffness
304 anisotropy, the SEM results of specimens CWD and CDD before compression were used to
305 characterise the directional distributions of soil particles/aggregates. Fig. 11(a) to (c) show the
306 procedures on the identification of particle/aggregate direction. Firstly, the SEM images were
307 imported into the software ImageJ for the identification of particle/aggregate edges (see Fig.
308 11(b)). Afterwards, particles/aggregates were fitted by ellipse as shown in Fig. 11(c) (Chow et
309 al., 2019; Chen et al., 2023). The length and orientation of these ellipses were summarised by

310 the ImageJ software, and the wind rose diagrams for particle/aggregate direction distributions
311 are given in Fig. 11(d). Barton (1974) suggested that at least 400-500 particles should be
312 identified to provide a representative fabric orientation. Therefore, approximately 60 SEM
313 images (about 700-800 particles/aggregates) were analysed in each wind rose diagram. As
314 expected, uniform directional distributions are identified for both specimens in the horizontal
315 plane. In the vertical plane, the particle/aggregate tends to lie horizontally, suggesting a
316 horizontal orientation for both specimens. The horizontally orientated particles/aggregates are
317 induced by the larger stress in the vertical direction than in the horizontal direction during 1-D
318 compaction. More importantly, more particles tend to lie horizontally for the dry of optimum
319 specimen in the vertical plane than the wet of optimum specimen. The more horizontally
320 orientated fabrics for the dry of optimum specimen lead to more anisotropic stiffness than the
321 wet of optimum specimen, as shown in Fig. 6.
322
323 **Discussion**
324 As shown in previous sections, soil structure significantly affects the stiffness. Based on
325 the above results, the ratio of normalised stiffness $\left[\frac{G_{hv}}{f(e)}\right]_i / \left[\frac{G_{hv}}{f(e)}\right]_j$ is calculated, where the
326 subscriptions "i" and "j" refer to the specimens with initially larger and smaller $G_{hv}/f(e)$,
327 respectively. Fig. 12 summarises the variation of $\left[\frac{G_{hv}}{f(e)}\right]_i / \left[\frac{G_{hv}}{f(e)}\right]_j$ with respect to the normalised
328 stress p'/p'_{yi}, where p'_{yi} is the yield stress of the specimen with initially larger stiffness. The
329 influence of compaction water content and dry density is considered. Before compression, the
330 $G_{hv}/f(e)$ increases with decreasing compaction water content and increasing dry density.

However, these two trends are reversed with increasing stress, with the value of $\left[\frac{G_{hv}}{f(e)}\right]_i / \left[\frac{G_{hv}}{f(e)}\right]_j$ being larger and smaller than 1 before and after compression, respectively. Based on the SM, SEM and MIP results, the trend reversal is most likely because of structure evolutions, where the interparticle contacts are more strengthened and pores are more compressed in the initially softer specimens than the initially stiffer specimens. Further inspections of Fig. 12 show that $\left[\frac{G_{hv}}{f(e)}\right]_i / \left[\frac{G_{hv}}{f(e)}\right]_j = 1$ is obtained when p'/p'_{yi} falls in the range of 2 to 3. The observation suggests that the soil structure is significantly altered at this stress range, inducing remarkable changes in soil stiffness.

Moreover, this study suggests that both A (A_{hh} and A_{hv}) and n (n_h and n_v) in equation (2) vary with structure (see Fig. 8). The varied A and n indicate that the common assumption in the literature (i.e., only A accounts for structure effects but n is constant and structure-independent) may not be appropriate. One potential method to modify equation (2) with incorporating structure effects is to correlate both A and n to a structure parameter while considering the structure evolutions with stress. The adoption of structure-dependent A and n is recommended for predicting ground movement and analysing the serviceability limit states of earthen structures.

Conclusions

This study investigated the evolution of anisotropic stiffness and structure of saturated and compacted loess during isotropic compression. The influence of compaction condition (water content and dry density) was explored. The main conclusions are summarised as follows:

Before compression, the specimen becomes stiffer with decreasing compaction water content and increasing compaction dry density. The $G_{hv}/f(e)$ of dry optimum specimen is larger than that of wet of optimum, which is because the aggregated structure (dry of optimum) is stiffer than the structure featured by colds (wet of optimum). Due to the larger compaction effort, denser specimens have larger $G_{hv}/f(e)$ than looser specimens.

It is newly found in this study that the $G_{hv}/f(e)$ of initially stiffer specimens becomes smaller than that of initially softer specimens when the stress exceeds 2 to 3 times the yield stress of initially stiffer specimens. After compression, larger $G_{hv}/f(e)$ is observed in the initially softer specimens (the specimens compacted at larger water content and smaller dry density). This is likely because interparticle contacts are more strengthened and pores are more compressed in the initially softer specimens. This observation provides a possible explanation for why the soil structure can induce either larger or smaller stiffness observed in the literature. Moreover, using structure-dependent A and n gives more reliable predictions when calculating the deformation of geostructures.

The stiffness anisotropy is more significant with increasing compaction dry density and decreasing compaction water content. Based on the directional distribution results (i.e., wind rose diagram), the more significant anisotropy is because of the more orientated fabrics in the specimen compacted at higher density and lower water content.

Declaration of Competing Interest

The authors declared that there is no conflict of interest.

Data availability

SEM images analysed during wind rose diagram are publicly available from *figshare* server at *https://figshare.com/s/a0c91e3adc99da5236c2*. Data generated or analyzed for other results are provided in full within the article.

Acknowledgements

This work is supported by the National Science Foundation of China through research grants 52022004 and 52279109. The authors also would like to thank the Research Grants Council of the HKSAR for providing financial support through grant 15205721.

References

Akin, I. D., Potter, L. S. and Edil, T. B. (2021). Implications of interparticle forces on resilient and shear modulus of unsaturated compacted kaolinite. *Journal of Geotechnical and Geoenvironmental Engineering* **147(12)**:04021152.

Alonso, E. E., Pinyol, N. M. and Gens, A. (2013). Compacted soil behaviour: initial state, structure and constitutive modelling. *Géotechnique* **63(6)**:463–478.

Asadi, M. B., Asadi, M. S., Orense, R. P. and Pender, M. J. (2020). Small-strain stiffness of natural pumiceous sand. *Journal of Geotechnical and Geoenvironmental Engineering* **146(6)**:06020006.

ASTM. (1998). Standard test method for particle-size analysis of soils. D422-63(1998),

American Society for Testing and Materials.

ASTM. (2017a). Standard practice for classification of soils for engineering purposes (unified soil classification system). D2487-17, American Society for Testing and Materials.

ASTM. (2017b). Standard test methods for liquid limit, plastic limit, and plasticity index of soils. D4318-17e1, American Society for Testing and Materials.

ASTM. (2023). Standard test methods for specific gravity of soil solids by the water displacement method. D854-23, American Society for Testing and Materials.

Atkinson, J. H. (2000). Non-linear soil stiffness in routine design. *Géotechnique* **50(5)**:487–508.

Barton, C. M. (1974). Micromorphological soil-investigation work of Dr. Lafeber. In *Proceedings of The International Working Meeting on Soil Micromorphology*, pp. 1–19.

Bentil, O. T. and Zhou, C. (2024). Suction and anisotropy effects on the stiffness characteristics of a compacted lateritic clay from small to large strains. *Canadian Geotechnical Journal* **61(10)**:2049–2063.

Cascante, G. and Santamarina, J. (1996). Interparticle contact behavior and wave propagation. *Journal of Geotechnical Engineering* **122(10)**:831–839.

Chen, Z. J., Zhao, R. D., Chen, W. B., Wu, P. C., Yin, J. H. and Feng, W. Q. (2023). Effects of temperature on the time-dependent compression and shear behaviour of a soft marine clayey soil. *Engineering Geology* **314**:107005.

Chow, J. K., Li, Z. F. and Wang, Y. H. (2019). Comprehensive microstructural

characterizations of 1-D consolidated kaolinite samples with fabric tensors and pore elongation factors. *Engineering Geology* **248**:22–33.

Clayton, C. R. I. (2011). Stiffness at small strain: research and practice. *Géotechnique* **61(1)**:5–37.

Dai, B. L. and Zhou, C. (2025). Characteristics of permanent strain accumulation and resilient modulus of unsaturated and structured soil under repeated loads. *Journal of Geotechnical and Geoenvironmental Engineering* **151(12)**:04025157.

Delage, P., Audiguier, M., Cui, Y. J. and Howat, M. D. (1996). Microstructure of a compacted silt. *Canadian Geotechnical Journal* **33(1)**:150–158.

Gasparre, A., Nishimura, S., Coop, M. R. and Jardine, R. J. (2007). The influence of structure on the behaviour of London Clay. *Géotechnique* **57(1)**:19–31.

Hasan, A. M. and Wheeler, S. J. (2014). Influence of compaction procedure on elastic anisotropy. In *Proceedings of 5th International Conference on Unsaturated Soils* **vol. 1**, pp. 285–289.

Iwasaki, T. and Tatsuoka, F. (1977). Effects of grain size and grading on dynamic shear moduli of sands. *Soils and Foundations* **17(3)**:19–35.

Jamiolkowski, M., Lancellotta, R. and Lo Presti, D. C. F. (1995). Remarks on the stiffness at small strains of six Italian clays. In *Proceedings of Pre-failure Deformation of Geomaterials* **vol. 2**, pp. 12–14.

Khosravi, A., Hashemi, A., Ghadirianniari, S. and Khosravi, M. (2020). Variation of small-strain shear modulus of unsaturated silt under successive cycles of drying and wetting.

436 *Journal of Geotechnical and Geoenvironmental Engineering* **146(7)**:04020050.
437 Lee, E. (2004). The compression behaviour of transitional soils. *Master's thesis, Imperial*
438 *College London, London, UK.*
439 Lee, J. S. and Santamarina, J. C. (2005). Bender elements: performance and signal
440 interpretation. *Journal of Geotechnical and Geoenvironmental Engineering*
441 **131(9)**:1063–1070.
442 Liu, X., Zhang, N. and Lan, H. X. (2019). Effects of sand and water contents on the small-
443 strain shear modulus of loess. *Engineering Geology* **260**:105202.
444 Liu, Z., Liu, F. Y., Ma, F. L., Wang, M., Bai, X. H., Zheng, Y. L., Yin, H. and Zhang, G. P.
445 (2016). Collapsibility, composition, and microstructure of loess in China. *Canadian*
446 *Geotechnical Journal* **53(4)**:673–686.
447 Lu, J., Wang, T. H., Cheng, W. C., Yang, T. and Luo, Y. (2019). Permeability anisotropy of
448 loess under influence of dry density and freeze-thaw cycles. *International Journal of*
449 *Geomechanics* **19(9)**:04019103.
450 Mancuso, C., Vassallo, R. and d'Onofrio, A. (2002). Small strain behavior of a silty sand in
451 controlled-suction resonant column torsional shear tests. *Canadian Geotechnical*
452 *Journal* **39(1)**:22–31.
453 Martins, F. B., Bressani, L. A., Coop, M. R. and Bica, A. V. D. (2001). Some aspects of the
454 compressibility behaviour of a clayey sand. *Canadian Geotechnical Journal*
455 **38(6)**:1177–1186.
456 Mitaritonna, G., Amorosi, A. and Cotecchia, F. (2014). Experimental investigation of the

457 evolution of elastic stiffness anisotropy in a clayey soil. *Géotechnique* **64(6)**:463–475.
458 Mitchell, J. K. and Soga, K. (2005). Fundamentals of soil behavior. John Wiley and Sons, New
459 York.
460 Mu, Q. Y., Dai, B. L. and Zhou, C. (2023). A constitutive model for structured soils under
461 saturated and unsaturated conditions. *International Journal for Numerical and*
462 *Analytical Methods in Geomechanics* **47(14)**:2562–2586.
463 Mu, Q. Y., Dong, H., Liao, H. J., Zhou, C., Li, S. B. and Zhang, J. W. (2022). Effects of in situ
464 wetting-drying cycles on the mechanical behaviour of an intact loess. *Canadian*
465 *Geotechnical Journal* **59(7)**:1281–1284.
466 Muñoz-Castelblanco, J. A., Pereira, J. M., Delage, P. and Cui, Y. J. (2012). The water retention
467 properties of a natural unsaturated loess from northern France. *Géotechnique* **62(2)**:95–
468 106.
469 Ng, C. W. W. and Menzies, B. K. (2007). Advanced unsaturated soil mechanics and
470 engineering. Taylor and Francis.
471 Ng, C. W. W., Xu, J. and Yung, S. Y. (2009). Effects of wetting-drying and stress ratio on
472 anisotropic stiffness of an unsaturated soil at very small strains. *Canadian Geotechnical*
473 *Journal* **46(9)**:1062–1076.
474 Ng, C. W. W. and Yung, S. Y. (2008). Determination of the anisotropic shear stiffness of an
475 unsaturated decomposed soil. *Géotechnique* **58(1)**:23–35.
476 Oualmakran, M., Mercatoris, B. C. N. and François, B. (2016). Pore-size distribution of a
477 compacted silty soil after compaction, saturation, and loading. *Canadian Geotechnical*

478 *Journal* **53(12)**:1902–1909.

479 Oztoprak, S. and Bolton, M. D. (2013). Stiffness of sands through a laboratory test database.

480 *Géotechnique* **63(1)**:54–70.

481 Sadeghi, H. (2016). A micro-structural study on hydro-mechanical behavior of loess. *PhD*

482 *Thesis, Hong Kong University of Science and Technology.*

483 Tang, A. M., Vu, M. N. and Cui, Y. J. (2011). Effects of the maximum soil aggregates size and

484 cyclic wetting-drying on the stiffness of a lime-treated clayey soil. *Géotechnique*

485 **61(5)**:421–429.

486 Todisco, M. C., Coop, M. R. and Pereira, J. M. (2018). Fabric characterisation in transitional

487 soils. *Granular Matter* **20(2)**:1–12.

488 Vahedifard, F., Thota, S. K., Cao, T. D., Samarakoon, R. A. and McCartney, J. S. (2020).

489 Temperature-dependent model for small-strain shear modulus of unsaturated soils.

490 *Journal of Geotechnical and Geoenvironmental Engineering* **146(12)**:04020136.

491 Viggiani, G. and Atkinson, J. H. (1995). Stiffness of fine-grained soil at very small strains.

492 *Géotechnique* **45(2)**:249–265.

493 Wang, F. T., Li, D. Q., Du, W. Q., Zarei, C. and Liu, Y. (2021). Bender element measurement

494 for small-strain shear modulus of compacted loess. *International Journal of*

495 *Geomechanics* **21(5)**:04021063.

496 Wang, J. T., Kong, L. W., Yan, J. B. and Zhou, Z. H. (2022). Comparative investigation on

497 small-strain stiffness characteristics of undisturbed and compacted highly weathered

498 granites at various densities. *Geofluids* **2022**:1–17.

499 Xu, L. and Coop, M. R. (2017). The mechanics of a saturated silty loess with a transitional
500 mode. *Géotechnique* **67(7)**:581–596.
501 Ying, Z., Cui, Y. J., Benahmed, N. and Duc, M. (2021). Changes of small strain shear modulus
502 and microstructure for a lime-treated silt subjected to wetting-drying cycles.
503 *Engineering Geology* **293**:106334.
504 Zhan, T. L. T., Yang, Y. B., Chen, R., Ng, C. W. W. and Chen, Y. M. (2014). Influence of clod
505 size and water content on gas permeability of a compacted loess. *Canadian*
506 *Geotechnical Journal* **51(12)**:1468–1474.
507 Zhou, C., Ng, C. W. W. and Chen, R. (2015). A bounding surface plasticity model for
508 unsaturated soil at small strains. *International Journal for Numerical and Analytical*
509 *Methods in Geomechanics* **39(11)**:1141–1164.
510 Zuo, L., Xu, L., Baudet, B. A., Gao, C. Y. and Huang, C. (2024). Small-strain shear stiffness
511 anisotropy of a saturated clayey loess. *Géotechnique* **74(4)**:325–336.
512

List of tables

List of figures

Table 1. Geotechnical index of tested material

Parameter	Value
Specific gravity, G_s	2.67
Grain-size distribution: % (ASTM, 1998)	
Clay fraction (<0.005 mm)	25.1
Silt fraction (0.005 mm - 0.075 mm)	73.7
Sand fraction (0.075 mm - 4.75 mm)	1.2
Gravel fraction (4.75 mm - 75 mm)	0
Liquid limit, w_L: %	31
Plastic limit, w_p: %	18
Plasticity index: %	13
Unified Soil Classification System (ASTM, 2017a)	CL

Table 2. Test program and specimen initial states

Specimen ID	Vertical stress during preparation σ_{v0}: kPa	Initial water content w_0: %	Initial dry density ρ_{d0}: g/cm^3	Initial void ratio e_0
CDL	220	13.5	1.19	1.22
CDD	500	13.3	1.50	0.78
COL	130	15.3	1.20	1.22
COD	250	15.6	1.50	0.78
CWL	35	18.5	1.23	1.17
CWD	170	18.6	1.52	0.75

Notes:
'C' is compacted; 'D, O and W' indicate dry of optimum , the optimum and wet of the optimum, respectively; 'L and D' represent the looser and denser states, respectively.

Table 3. Specimens for microstructure analysis

Specimen identity	Soil state	Analysis method
CDD	Before and after compression	SM, SEM and MIP
CWL	Before and after compression	SEM and MIP
CWD	Before and after compression	SM, SEM and MIP

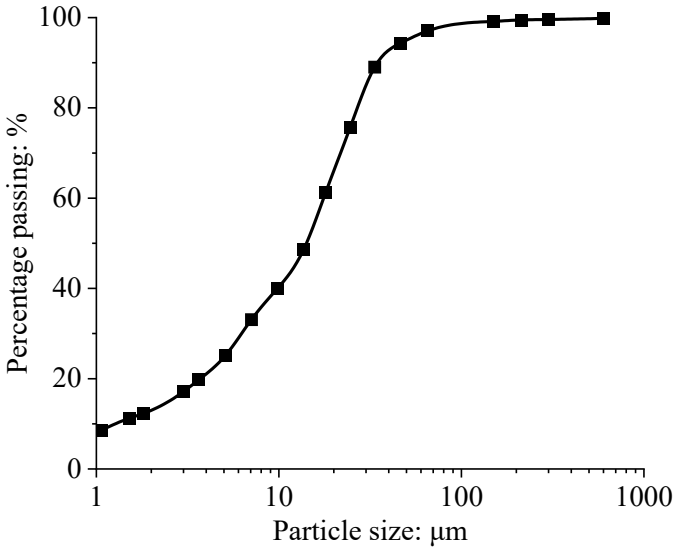

(a)

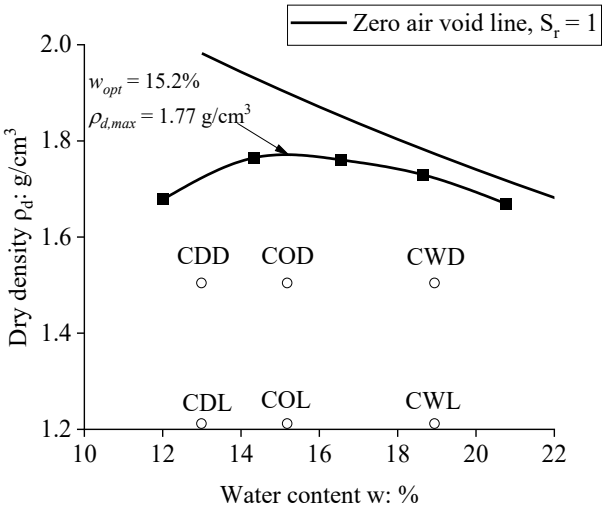

(b)

Fig. 1. Basic properties of tested loess: (a) particle size distribution; (b) compaction curve and specimen initial states

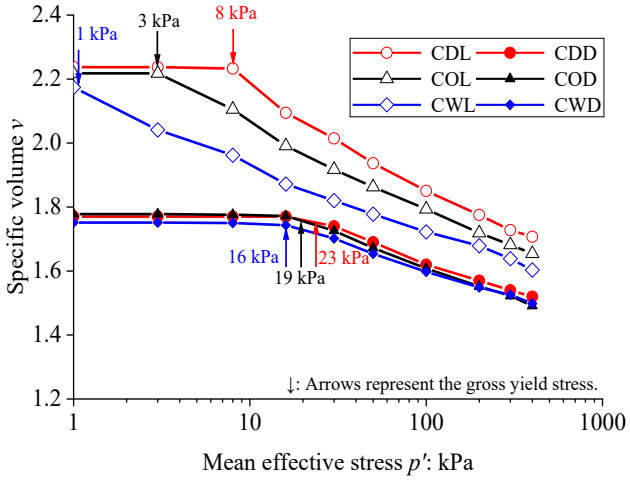

Fig. 2. Isotropic compression curves

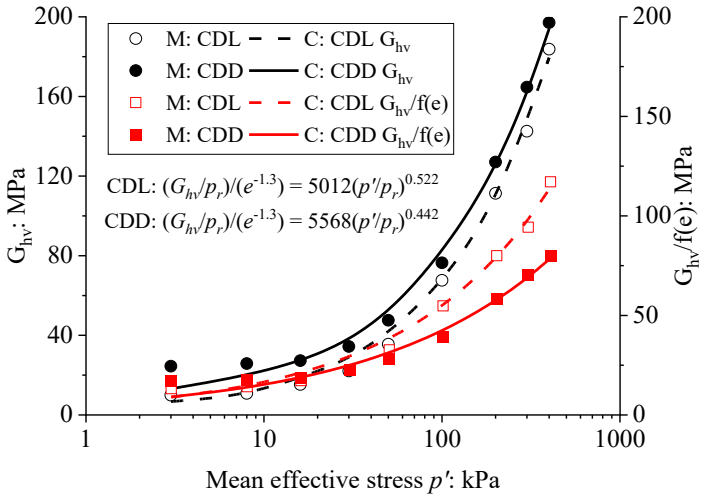

(a)

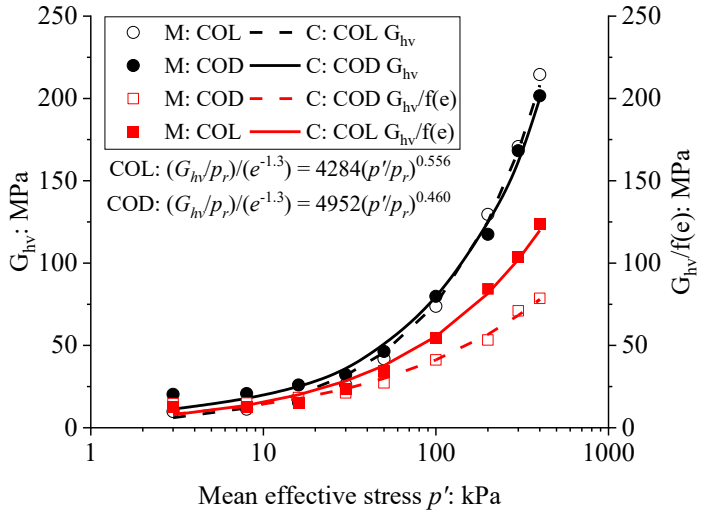

(b)

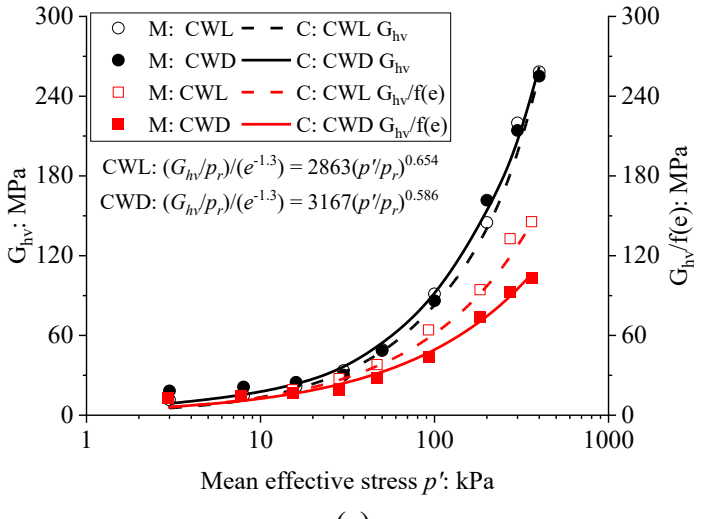

(c)

Fig. 3. Effects of compaction dry density on the stiffness G_{hv} and normalised stiffness $G_{hv}/f(e)$: (a) dry of optimum; (b) optimum; (c) wet of optimum (M/C: measured/computed)

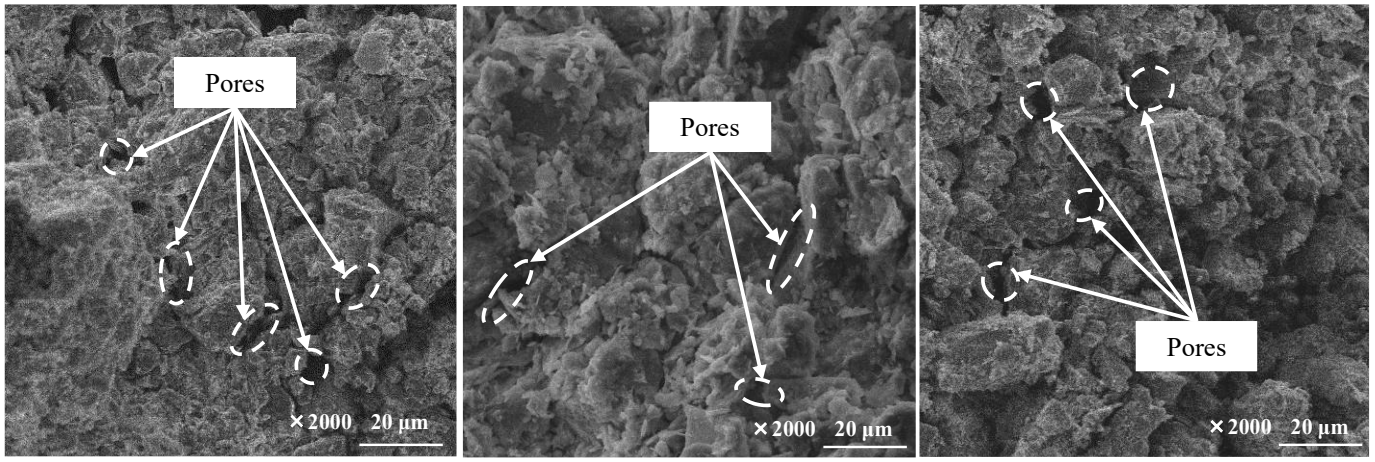

(a)

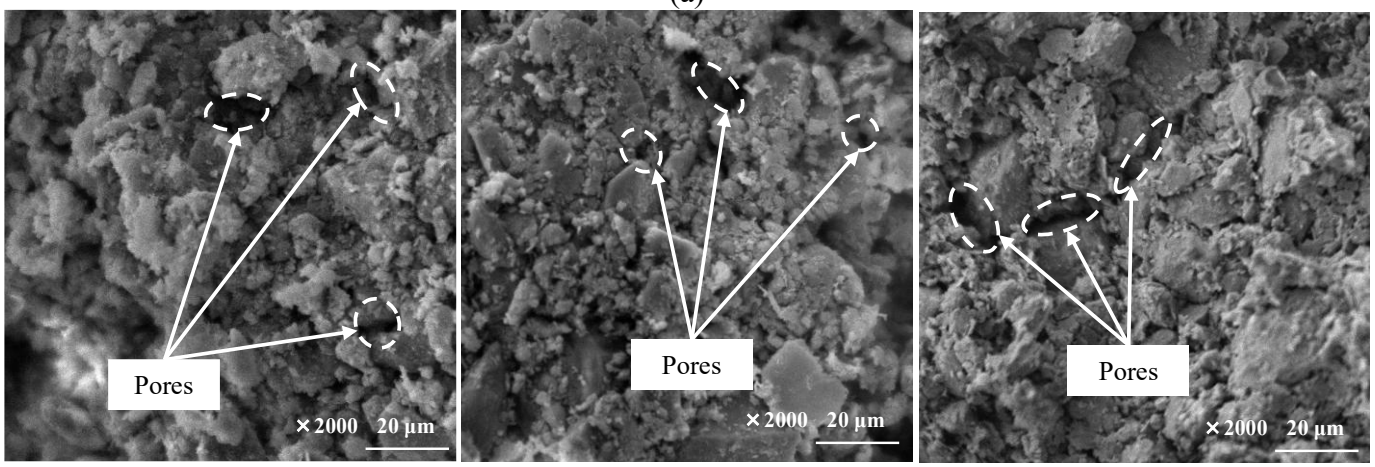

(b)

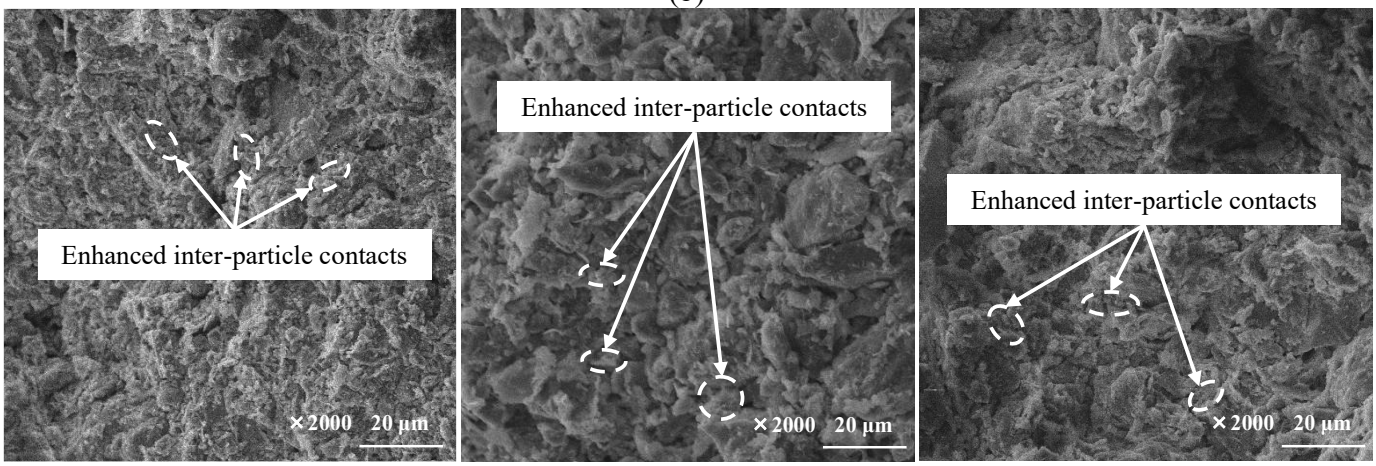

(c)

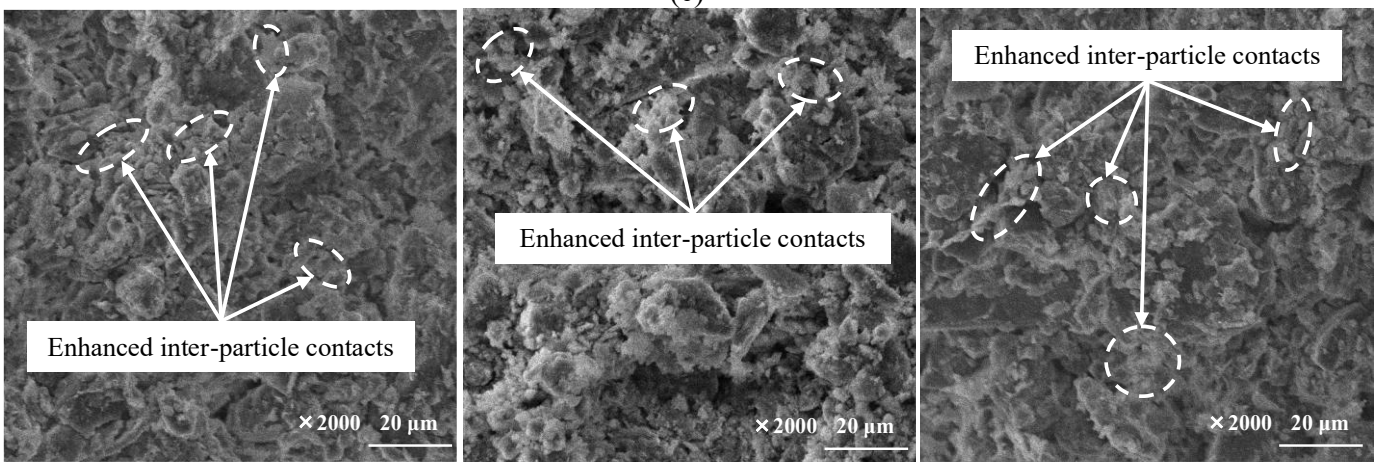

(d)

Fig. 4. SEM results of specimens with different compaction densities: (a) CWL before compression; (b) CWD before compression; (c) CWL after compression; (d) CWD after compression

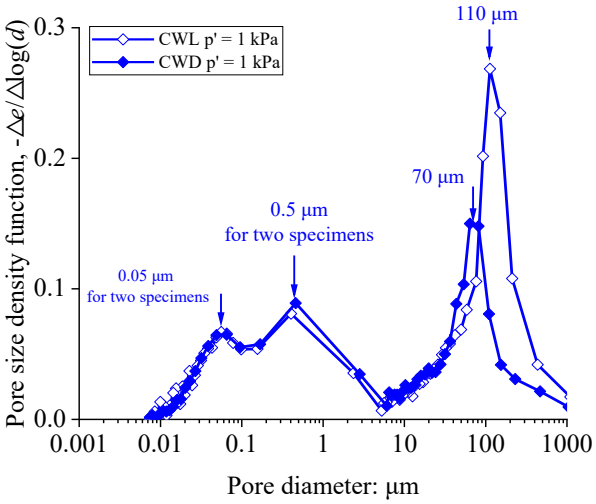

(a)

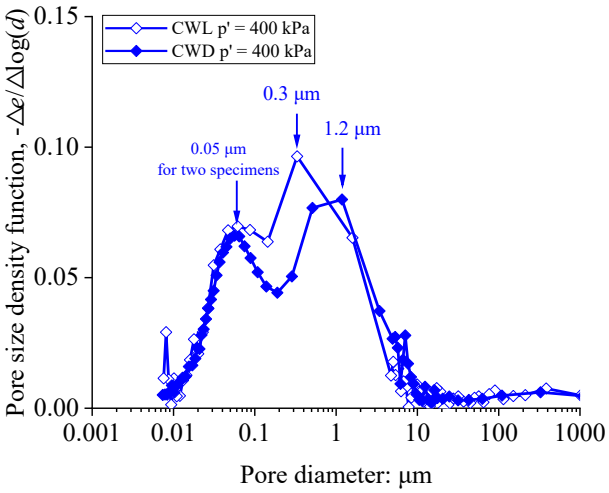

(b)

Fig. 5. MIP results of specimens with different compaction densities: (a) before compression; (b) after compression

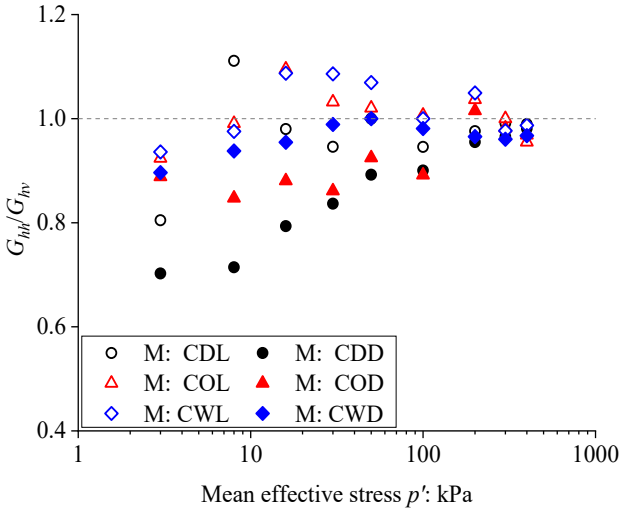

Fig. 6. Stiffness anisotropy G_{hh}/G_{hv} for compacted specimens

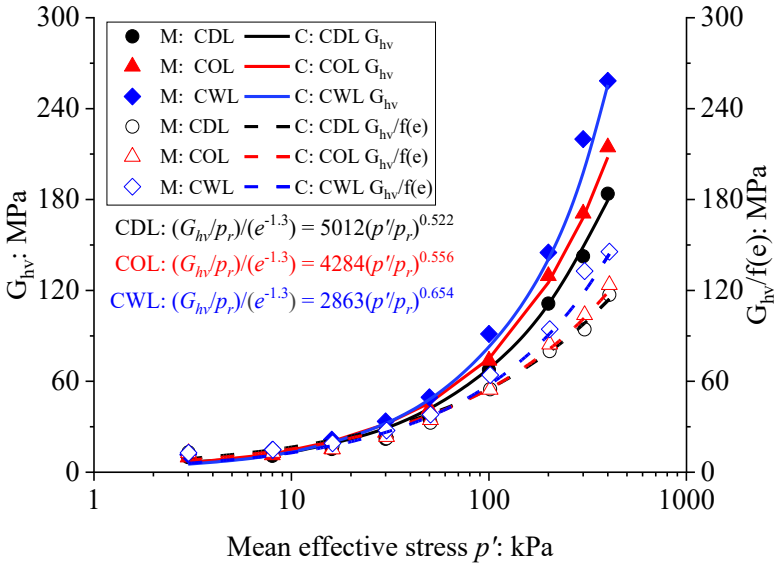

(a)

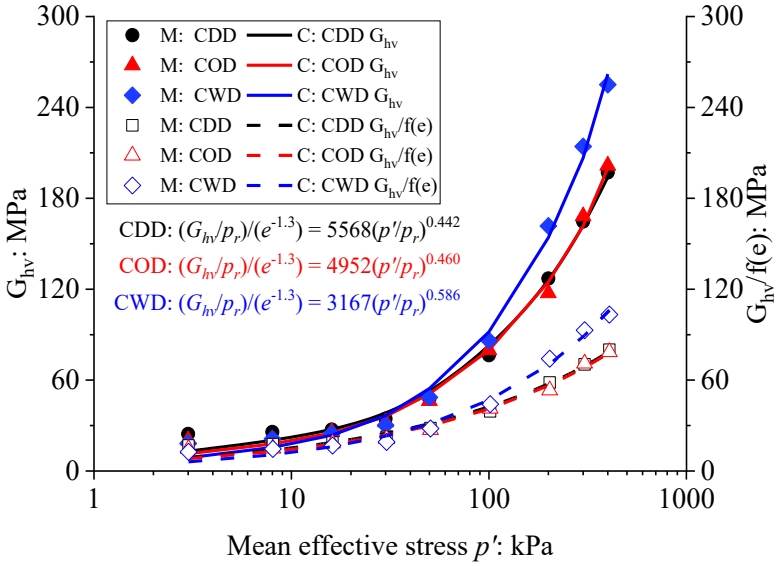

(b)

Fig. 7. Effects of compaction water content on the stiffness G_{hv} and normalised stiffness $G_{hv}/f(e)$: (a) looser state; (b) denser state

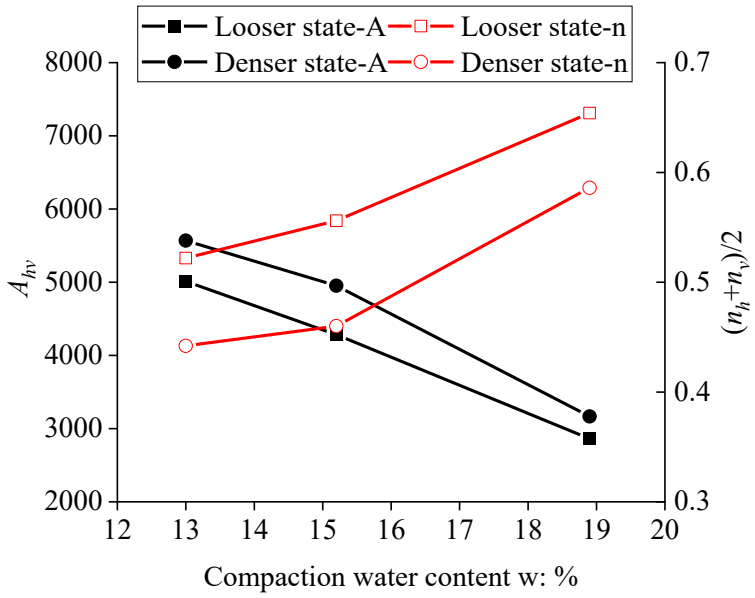

Fig. 8. Variations of parameters A_{hv} and $\frac{n_h+n_v}{2}$ with compaction water content

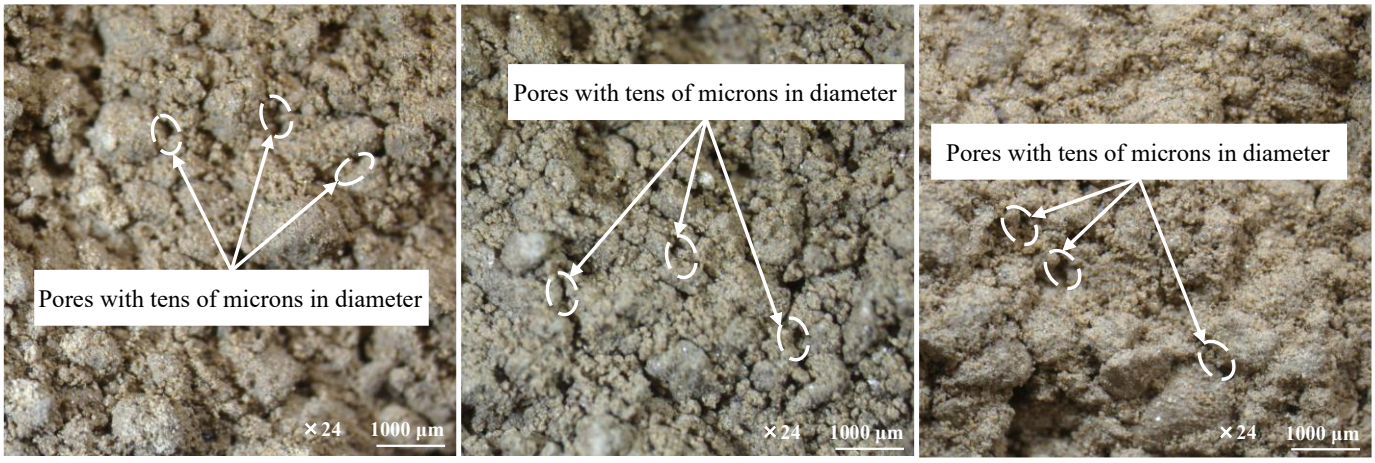

(a)

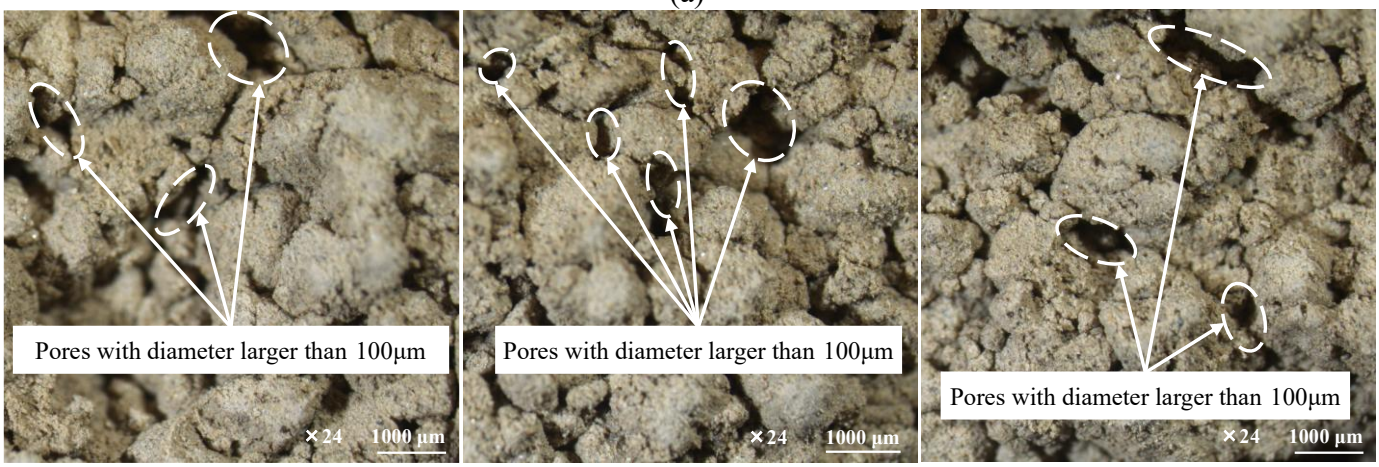

(b)

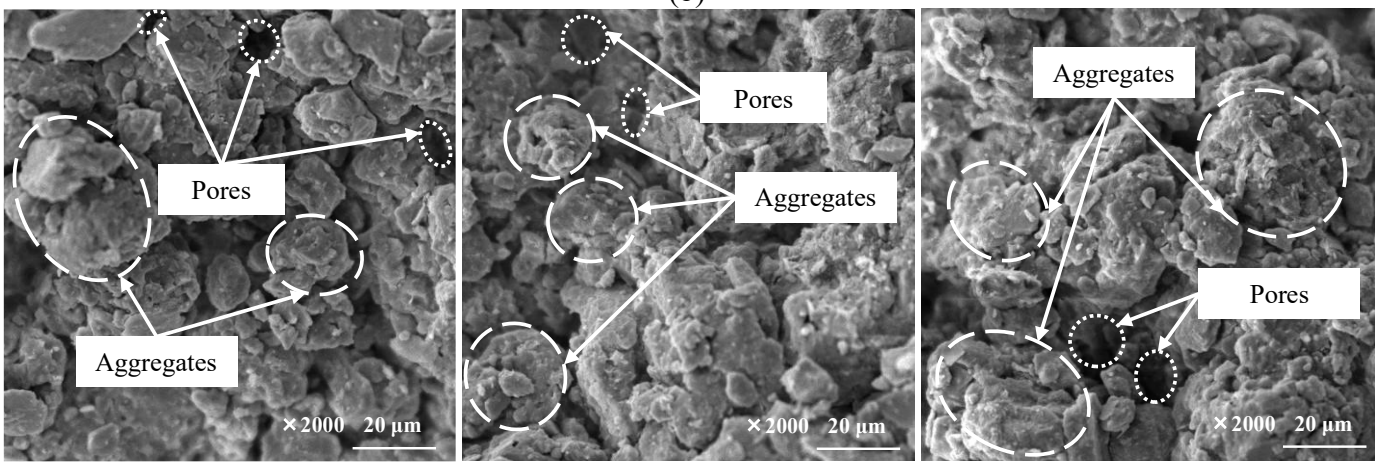

(c)

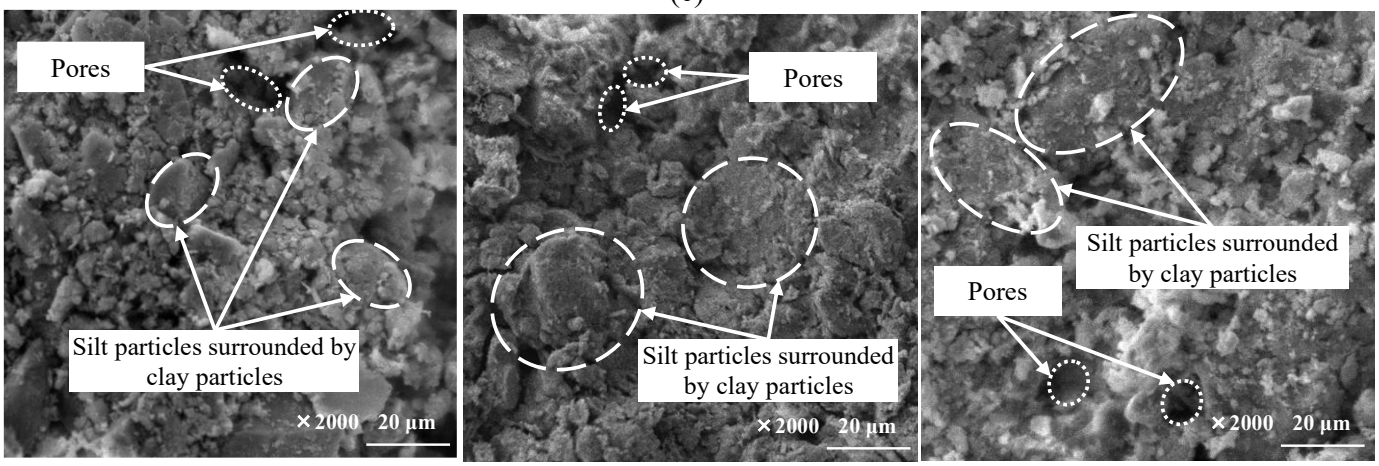

(d)

Fig. 9. SM and SEM results: (a) CDD-SM; (b) CWD-SM; (c) CDD-SEM; (d) CWD-SEM

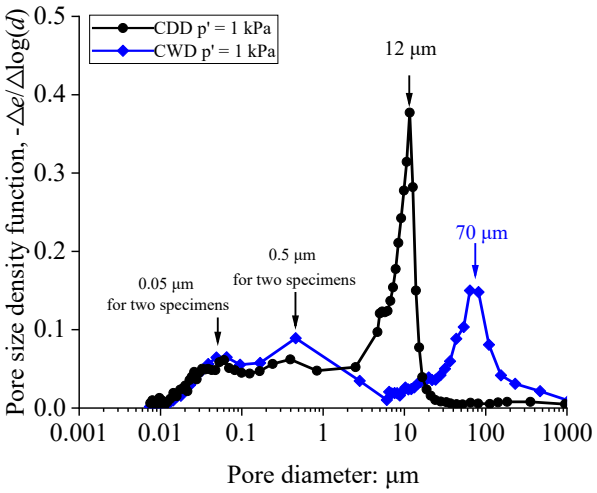

(a)

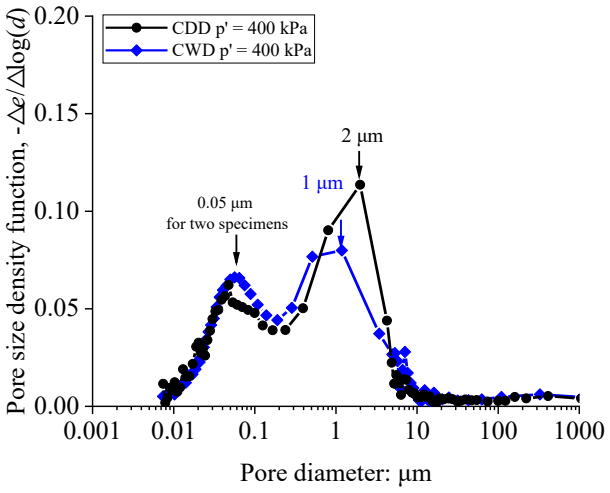

(b)

Fig. 10. MIP results of specimens with different compaction water contents: (a) before compression; (b) after compression

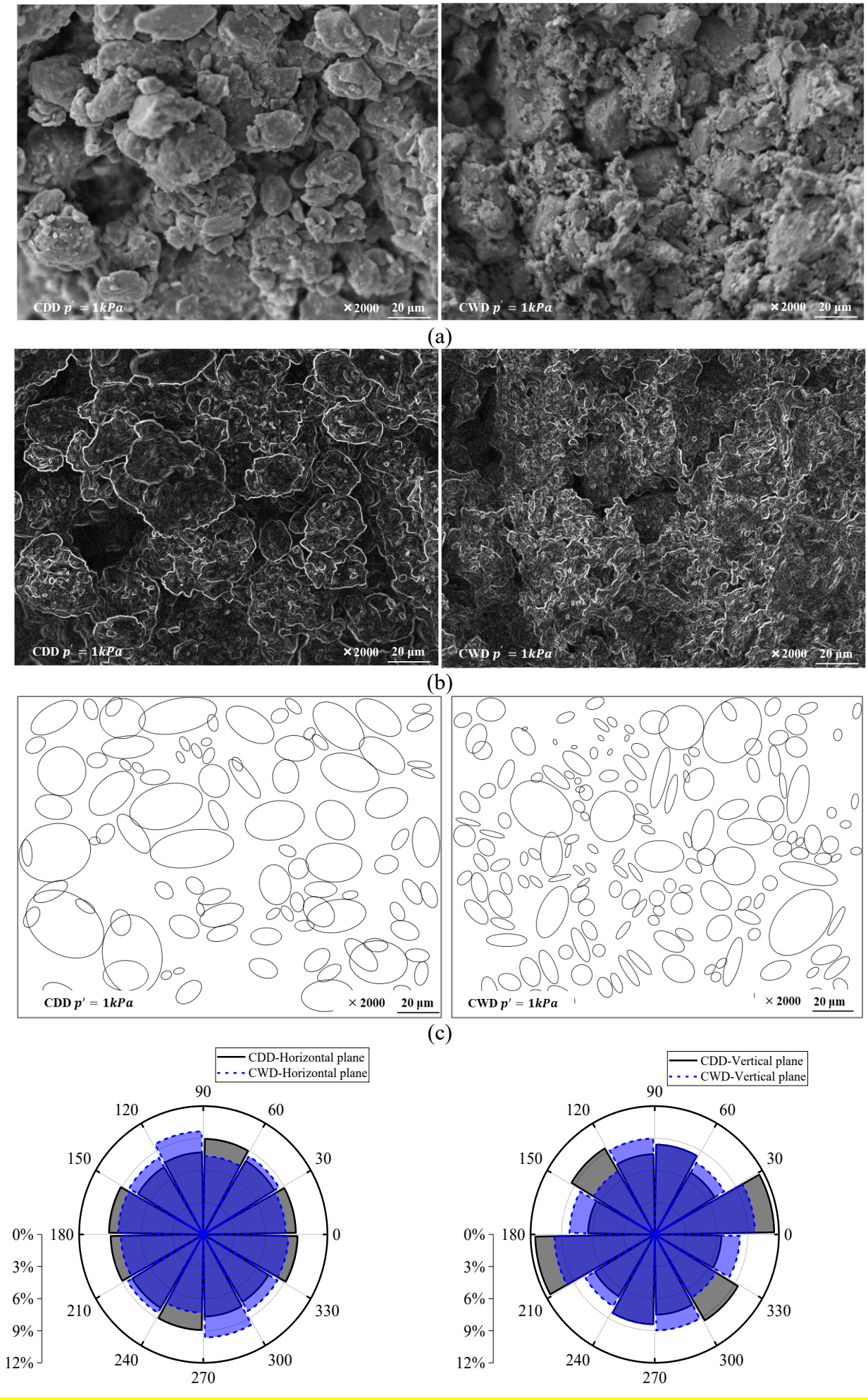

Fig. 11. The directional distribution of particle/aggregate for denser specimens: (a) SEM results; (b) edge identification; (c) ellipse fitting; (d) wind rose figures

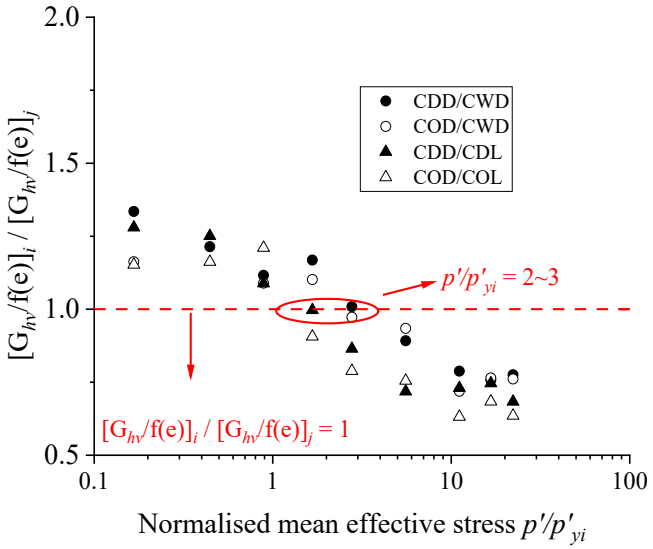

Fig. 12. The variation of normalised stiffness ratio with normalised mean effective stress